JOURNAL OF AIRCRAFT
Vol. 31, No. 2, March–April 1994

Vortex-Wing Interaction of a Close-Coupled Canard Configuration

Eugene L. Tu*
NASA Ames Research Center, Moffett Field, California 94035

The thin-layer Navier-Stokes equations are solved numerically to investigate the effects of canard vertical position on a close-coupled, canard-wing-body configuration at a transonic Mach number of 0.90 and angles of attack ranging from −2 to 12 deg. Canard-wing interactions are investigated for the canard positioned above, coplanar with, and below the wing (high-, mid- and low-canard positions, respectively). The computational results show favorable canard-wing interactions for the high- and midcanard configurations. The unfavorable lift and drag characteristics for the low-canard configuration are examined by analyses of the low-canard flowfield structure and found to be directly attributed to the interaction between the canard vortex and the wing surface. At relatively low angles of attack, the low-canard vortex passes under the wing surface and induces low pressures on the wing lower surface. As angle of attack is increased, the low-canard vortex impacts the wing surface and is split into two distinct vortices.

Introduction

THE use of canards in many advanced aircraft for control and improved aerodynamic performance has been the topic of continued research. In addition to providing rapid pitch control, the influence of canards on wing aerodynamics can often result in increased maximum lift and decreased trim drag. There are also unique dynamic performance characteristics for canard-configured aircraft coupled with the capability of present-day automatic control systems. The reduced or even negative static stability of canard configurations can lead to improved aircraft agility and maneuverability.

The proper positioning of canards is essential for optimized aerodynamic performance, as well as desirable stability and control characteristics. A wide variety of current aircraft utilize canards in different positions to accomplish these tasks. For example, the X-31 aircraft uses a long-coupled canard with a vertical offset (high canard) for pitch control and recovery.[1] During cruise, the X-31 canard becomes a neutral or "no-load" surface. On the other hand, the SAAB JAS 39 Gripen uses a short- (or close-) coupled high canard in maneuvering, cruise, and even landing rollout conditions.[2] The close-coupled canard of the X-29 forward-swept aircraft is integrated into the active control system and is used to maintain control of this inherently unstable aircraft.[3]

The vertical position of a close-coupled canard has a significant effect on the canard-wing aerodynamic interaction and, consequently, the aerodynamic performance of the aircraft. Proper utilization of canards requires an accurate understanding of the influence of canard positioning on the flow structure about the wing.

At moderate angles of attack, canards or wings with sharp leading edges exhibit flow separation at the leading edge due to the adverse pressure gradient on the leeward side. The flow structure of highly swept or delta canard-wing configurations is characterized by a canard downwash, which modifies the wing flowfield, and an interaction between the canard and wing vortex systems. The inboard wing flowfield is often dominated by the canard downwash, and the outboard is affected by the subsequent change in wing leading-edge vortex formation and the canard-wing vortex interaction. A schematic of a typical canard-wing vortex interaction is given in Fig. 1.

For a canard positioned with a vertical offset (high or low canard), the different locations of the canard wake and leading-edge vortex can significantly change the canard-wing flowfield from that of the midcanard case. These changes in the flowfield can affect both the aerodynamic performance as well as the stability and trim characteristics of a configuration. Additional flow features contributing to the complex flow structure of canard configurations include secondary, trailing-edge, and tip vortices, as well as regions of shock-induced or boundary-layer separation. A strong primary vortex often causes the formation of a strong secondary vortex which will affect

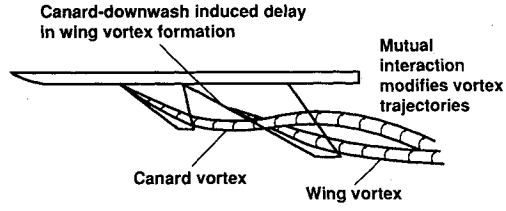

Fig. 1 Schematic of the canard-wing vortex interaction.

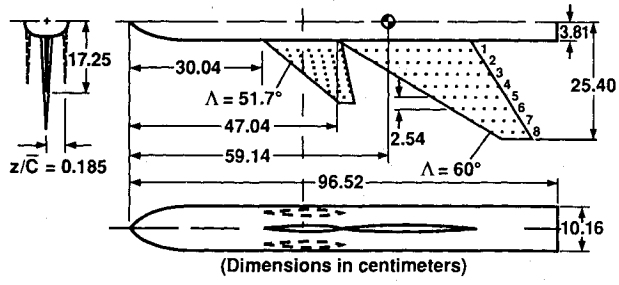

Canard	Wing	
AR = 4.12	AR = 2.5	Circular arc airfoil sections
C̄ = 14.83 cm	C̄ = 23.31 cm	maximum thickness
S = 288.73 cm² (exposed)	S = 1032.2 cm²	
Root chord = 17.92 cm	Root chord = 29.80 cm	Root = 6%
Tip chord = 3.59 cm	Tip chord = 6.77 cm	Tip = 4%

Fig. 2 Canard-wing-body geometry (canard positions $z/\bar{c} = +0.185$, 0.0, and −0.185 shown).

Received Sept. 8, 1992; revision received Jan. 19, 1993; accepted for publication Jan. 19, 1993.

*Research Scientist, Computational Aerosciences Branch, M/S 258-1. Member AIAA.

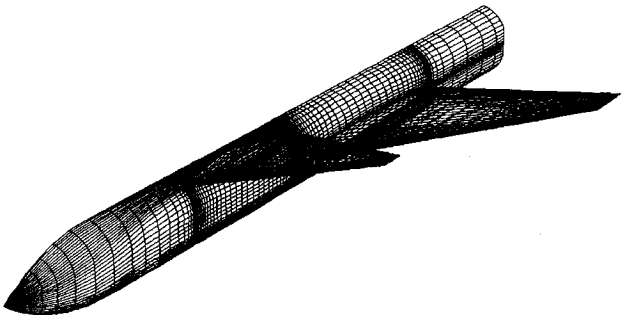

Fig. 3 Surface grid for the high-canard ($z/\bar{c} = +0.185$) configuration.

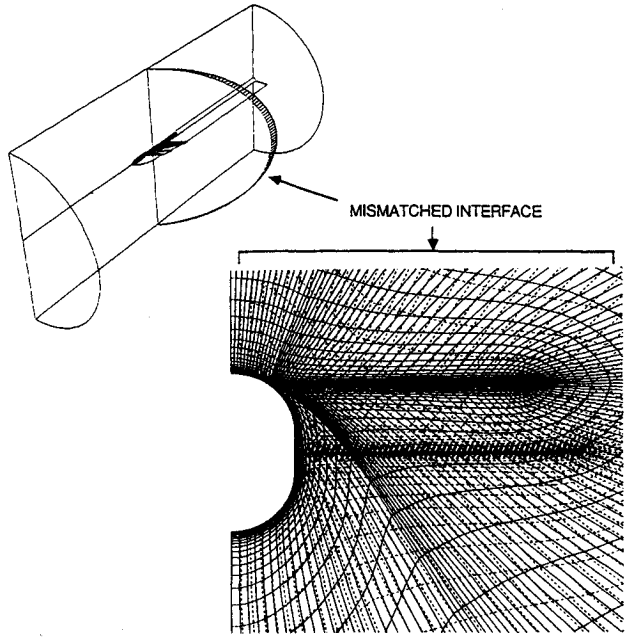

Fig. 4 Canard-wing-body flowfield grid topology and canard/wing mismatched interface for the high-canard.

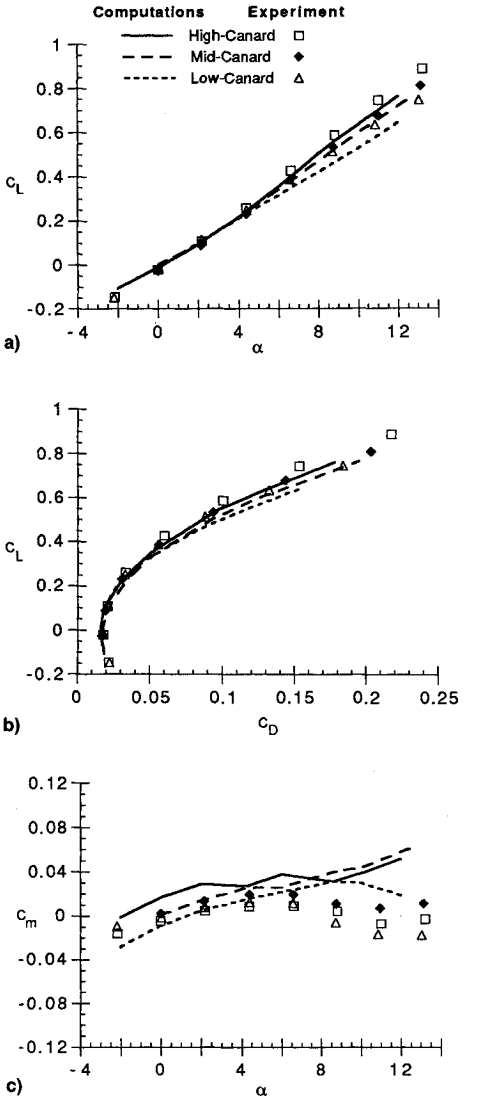

Fig. 5 Comparison of computational and experimental forces and moments for the high-, mid-, and low-canard configurations. M_∞ = 0.90, $Re_{\bar{c}}$ = 1.52 million: a) lift, b) drag, and c) pitching moment.

the surface pressures near the canard or wing leading edge. Furthermore, trailing-edge and tip vortices can interact with the leading-edge vortex as it convects downstream. Boundary-layer separation due to high angles of attack, or induced by a strong recovery shock, is also influenced by the presence of these vortices.

The use of canards for improved performance has been supported by numerous experimental studies as well as some recent computational studies. These studies are listed in detail in Ref. 4. Gloss and McKinney,[5] and Gloss[6,7] provided insight into the effects of canard geometry and positioning on the aerodynamic loading of a typical canard-wing-body geometry. Lacey[8] conducted an extensive four-volume experimental study on the effects of canard geometry, position, and deflection on aerodynamic loads in the subsonic to supersonic regimes. A series of experimental studies by Gloss and Washburn[9,10] provided detailed measurements of surface pressures—as well as integrated force quantities—on a variety of configurations and flow conditions near the transonic regime. More recent experimental studies by Er-El and Seginer,[11] Calarese,[12] and Oelker and Hummel[13] concentrated on the canard and wing vortex systems and provided details into the mechanisms of their interaction.

In particular, the studies by Gloss et al.[7,10] identified unfavorable characteristics for the low-canard configuration. Substantial loss of lift due to the interaction between the low-canard wake and the wing was experimentally measured. However, due to the nature of these studies, insufficient data were obtained to completely describe the canard-wing flowfield.

Computational fluid dynamics (CFD) has become a valuable tool for understanding the complex three-dimensional flow physics of canard configurations. A number of studies based on conformal mapping, linear and nonlinear vortex lattice methods, the transonic small perturbation (TSP) equation, and Euler equations have been performed and are listed in Ref. 4. However, to the author's best knowledge, no computational work has been performed using the Navier-Stokes equations to study the detailed effects of canard positioning on the canard-wing-body flowfield. Although viscous computations may not be required to capture the primary vortex structure for sharp leading-edge geometries, viscous modeling is essential to capture some of the other significant features such as vortex-induced secondary separations and other boundary-layer-type separations. With the emergence of faster computers and increased memory capacities, the Navier-Stokes equations can now be utilized.

Using an extension of the NASA Ames Research Center's Transonic Navier-Stokes (TNS) code,[14,15] the thin-layer Navier-Stokes equations are solved for the steady flow about a highly swept canard-wing-body configuration. Previous studies[4,16] by the author confirmed the suitability of the present method for accurately simulating coplanar canard-wing-body aerodynamics with canard deflections. Accuracy was demonstrated by extensive comparisons with experimental

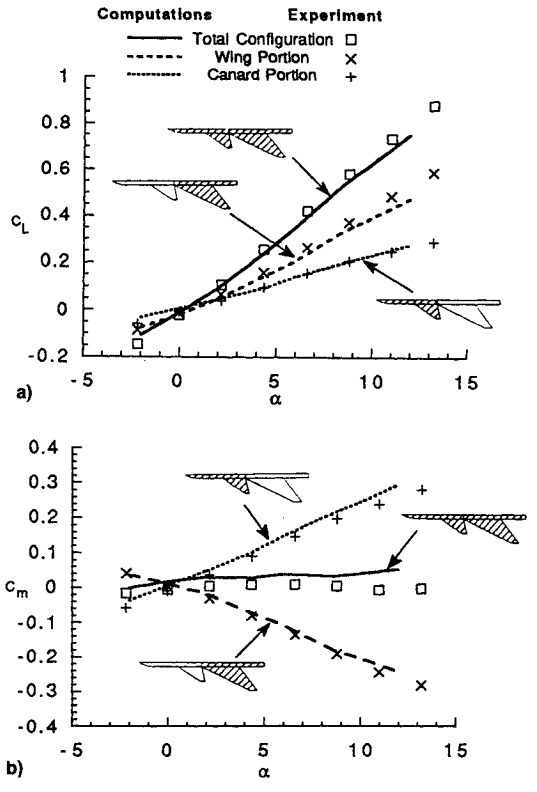

Fig. 6 Comparison of component lift and pitching moment curves for the high-canard configuration. $M_\infty = 0.90$, $Re_{\bar{c}} = 1.52$ million: a) component lift and b) component pitching moment.

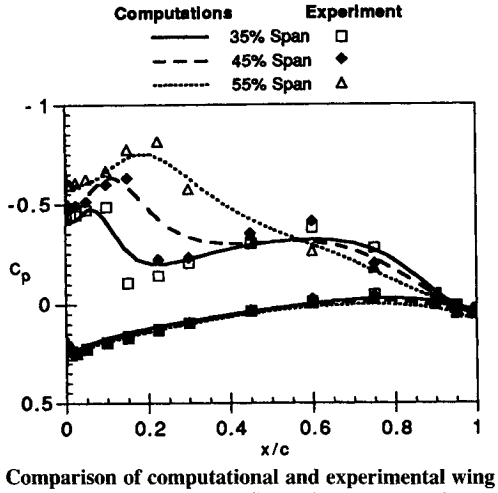

Fig. 7 Comparison of computational and experimental wing surface pressures for the high-canard configuration. $M_\infty = 0.90$, $\alpha = 8.55$ deg, $Re_{\bar{c}} = 1.52$ million.

surface pressure, force, and moment data. Furthermore, a grid refinement study was performed to resolve discrepancies in the baseline computational comparisons with experiment.

In the present study, the effect of canard vertical position on the longitudinal aerodynamic characteristics of a typical canard-wing-body geometry is investigated. Comparisons with available experimental data for the various canard position cases are favorable. Emphasis is placed on understanding the complex three-dimensional flowfield, including the canard-wing vortex interaction. The current application of the TNS code expands the capability for analysis of the complex aerodynamics of canard configurations.

Computational Modeling

Numerical Procedure

The TNS code is a Reynolds-averaged, thin-layer Navier-Stokes solver with structured zoning capability, and has been

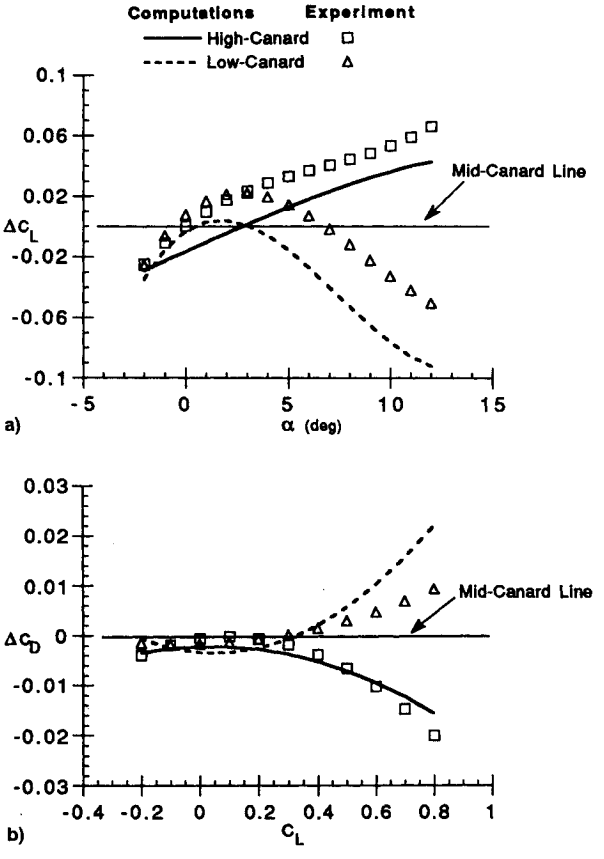

Fig. 8 Effect of canard vertical position on the incremental change in lift and drag coefficients. $M_\infty = 0.90$, $Re_{\bar{c}} = 1.52$ million: a) lift and b) drag.

demonstrated for a wide range of wing and aircraft configurations.[4,14-20] The original four-zone version of the TNS wing code has been used to solve for and investigate transonic viscous flows over various wing geometries, with and without wind-tunnel wall modeling.[14,17] The 16- and 27-zone versions of the TNS wing-fuselage (TNSWF) code have been successfully used to compute the flow about a modified F-16A wing-fuselage configuration[18] and a complete F-16A aircraft,[19] respectively. The code used in this study is a generalized version of the TNS code without restriction on grid topology or zonal arrangement. Recently, this general version of the TNS code has been applied to canard-wing-body configurations[4,16] and the F-16XL aircraft,[20] including inlet and diverter.

The Baldwin-Lomax algebraic eddy-viscosity model[21] is chosen to compute the effects of turbulence on the flow. Due to the vortex-dominated flow structures of the highly swept sharp leading-edge canard and wing, a modification to the original Baldwin-Lomax formulation is required. For this study, the Degani-Schiff modification,[22] as originally developed for crossflow-type separations, is employed. It is noted that with present-day CFD technology, higher-order eddy-viscosity models could easily be utilized and are readily available within the TNS code. However, with the lack of significant non-equilibrium or streamwise separation effects anticipated at the moderate angles of attack being investigated, the benefits for the current study of such higher-order models do not justify the increased computational costs. Further details about the TNS code, algorithm, zonal approach, and general performance are given in Refs. 14 and 15.

All results were computed using the supercomputer facilities at NASA Ames Research Center. A typical case required up to 4000 iterations from freestream conditions to converge, as defined by a three-order drop in residuals (L2 norm), stable configuration forces, and stable wing surface pressure distributions. Less than 1500 iterations were required for restart

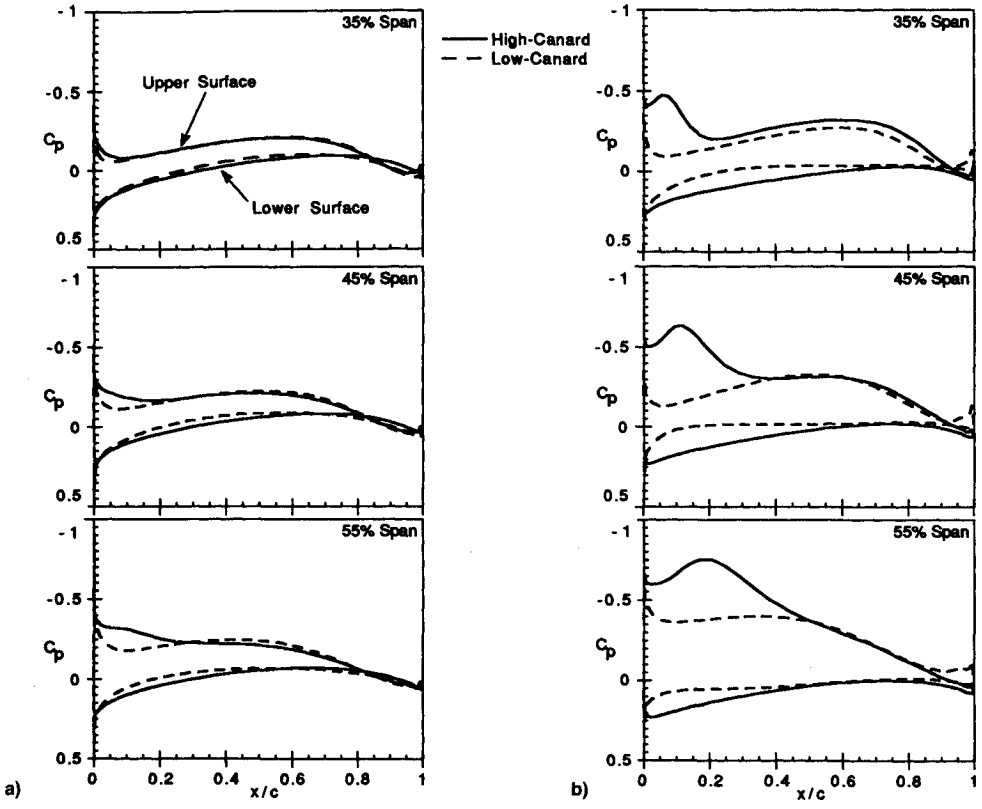

Fig. 9 Comparison of wing surface pressures for the high- and low-canard configurations. $M_\infty = 0.90$, $Re_{\bar{c}} = 1.52$ million: a) $\alpha = 4.27$ deg and b) $\alpha = 8.55$ deg.

cases with perturbations in angle of attack, Mach number, or Reynolds number.

Geometry Modeling and Grid Generation

The geometry in this study is based on the wind-tunnel model used by Gloss and Washburn,[7,9,10] and is illustrated in Fig. 2. In the wind-tunnel model, fairings were used to facilitate the vertical-offset canard. These fairings, which account for slight asymmetries in the experimental results for the midcanard case, are omitted in the current computational modeling. In the current study, the high- or low-canard geometry is created by vertically translating the midcanard. The surfaces of the canard are then extended into the upper or lower portion of the fuselage by linear extrapolations. The 6% thickness, given in Fig. 2, applies to the canard span station located at the same span as the wing root. The sting used for wind-tunnel mounting is modeled by extending the body, with its appropriate no-slip boundary condition, to the downstream boundary.

Using the S3D surface geometry and grid generation code,[23] the canard, wing, and body component surface geometries are modeled from their original analytical definitions. For the vertical-offset canard, the translation and extension of the canard, as well as the intersection of the canard with the fuselage is performed using S3D. Only the canard portion (canard plus forebody) of the surface grid is modified for the offset canard cases. An example of the surface grid for the high-canard case is shown in Fig. 3.

Since the canard-root trailing and wing-root leading edges are coincident, a mismatched zonal interface is used in the flowfield grid, separating the canard and wing portions. The 3DGRAPE[24] program is used to generate the canard and wing portions of the flowfield grid individually with a mutual overlapping interface analytically defined. The overall H-O topology grid, with the mismatched interface, for a typical high-canard case is given in Fig. 4. An expanded crossflow plane view of the interface is also shown with the solid lines indicating the downstream boundary of the high-canard portion grid. Since the mismatched interface surface is not necessarily a plane, trilinear interpolation—as formulated in Ref. 25—is used to transfer flow quantities from one zone to the other. For all of the cases presented in this study, the nonconservative form of interpolation is used and found to be sufficiently accurate. This accuracy is verified by the comparisons with experimental data and from previous studies[16] which used a similar technique for deflected canard configurations.

The resulting grid for a typical high- or low-canard case contains 10,150 points on the surface (total for half-model) and 730,000 flowfield points. Up to five zones stacked in the streamwise direction are used to minimize computer memory requirements. Except for the canard/wing portion interface, one-to-one grid matching is used on all interfaces. Since the current computations are performed in the transonic regime, the flowfield grid is extended upstream and downstream by approximately eight wing root-chord lengths, and in the radial direction by six wing span lengths.

Results and Discussion

Experimental Comparisons

Comparisons between computed results and experimental data[7,9] are made to validate the current method for accurately predicting the steady flowfield of vertical offset canard cases. All computations presented in this article are at a transonic Mach number M_∞ of 0.90, angles of attack α ranging from -4 to 12 deg, and canard vertical positions of $z/\bar{c} = +0.185$, 0.0, and -0.185 as measured from the wing plane (now referred to as high, mid and low canard, respectively). The Reynolds number based on the mean aerodynamic chord of the wing $Re_{\bar{c}}$ is 1.52 million. Because transition strips were used in the experiments at the body nose and leading edges of the canard and wing, the computations are performed assuming fully turbulent flow. Pitching moments are given about the c.g. location (Fig. 2).

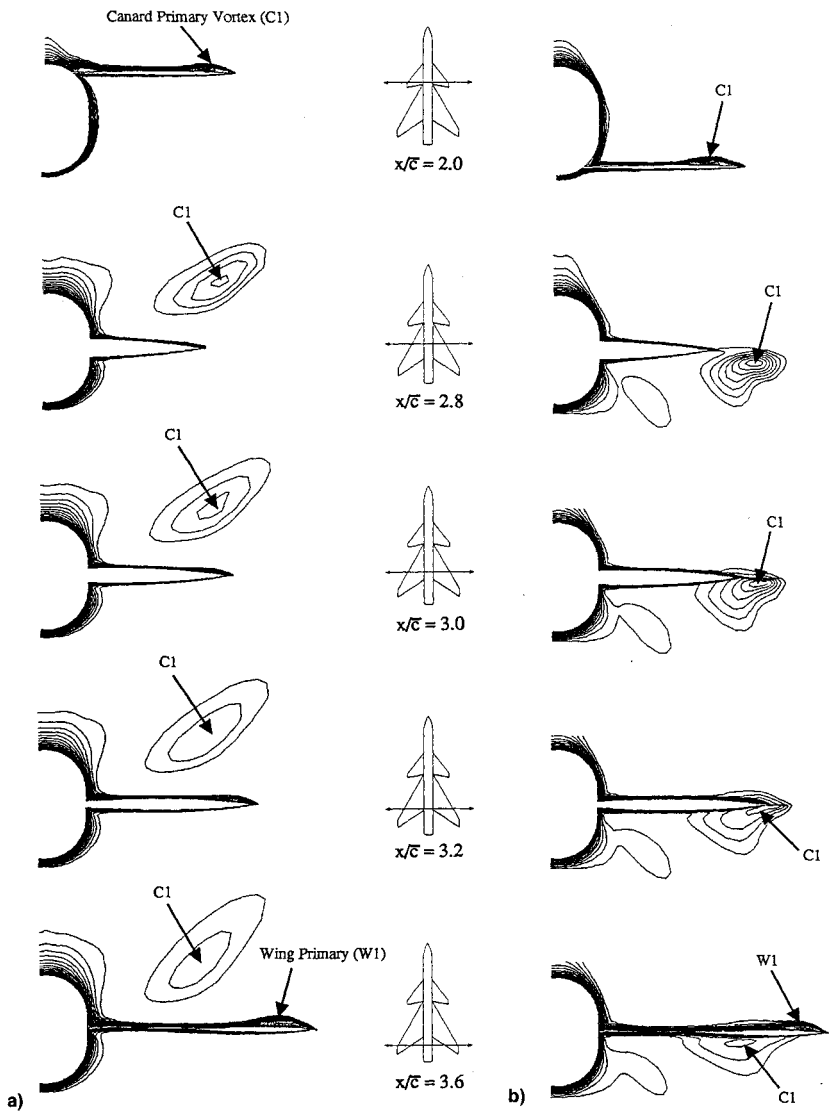

Fig. 10 Crossflow plane visualization of normalized total pressure contours for high- and low-canard configurations. $M_\infty = 0.90$, $\alpha = 4.27$ deg, $Re_c = 1.52$ million: a) high-canard and b) low-canard.

Details of the midcanard configuration, including surface pressure comparisons of canard-on and canard-off cases, can be found in Ref. 4. Comparisons of the lift, drag, and pitching moment curves with experimental data[7] are given in Fig. 5 for the high-, mid-, and low-canard cases. Figure 5a shows the nonlinearities in the high- and midcanard lift curves. At $\alpha > 4$ deg, significant differences are noted in the lift curves for the three canard positions. Although the absolute values of lift are slightly underpredicted by the computations, the relative differences are captured. Further investigation of the incremental changes due to canard vertical position is presented later in this article.

Figure 5b shows computed drag coefficient comparisons with experimental measurements. At the higher angles of attack, both computations and experiment show that the mid- and low-canard configurations exhibit a higher drag coefficient for a given lift coefficient. The discrepancies between experimental and computed pitching moments in Fig. 5c can be further investigated by a component breakdown of the lift and pitching moment curves.

Figures 6a and 6b illustrate lift and pitching moment curves, respectively, for two component regions of the high-canard configuration. The canard region consists of the canard and the body forward of the wing leading-edge root location (forebody). The wing region consists of the wing and the remaining aft-body (not including the sting).

The total lift curve in Fig. 6a is the sum of the canard and wing region lift curves. Figure 6a shows that the slight underprediction in total lift is primarily due to the computed wing portion lift which is expected to be more sensitive to the accurate prediction of the canard-wing interaction. The pitching moment curves in Fig. 6b show that the wing region exhibits statically stable characteristics, while the canard region pitching moment causes the total configuration to be approximately neutrally stable. Such characteristics are often typical of canard-configured aircraft and were also evident in the midcanard configurations.[4,16] Furthermore, Fig. 6b shows that the larger discrepancies in predicted pitching moments observed in Fig. 5c are primarily due to the summation of a large positive contribution of pitching moment (from the canard) with a large negative contribution (from the wing). Generally favorable comparisons in Figs. 6a and 6b between computations and experimental data indicate that the distribution of lift and moment between the component regions are captured well by the computations.

A comparison between computational and experimental[10] wing surface pressures is given in Fig. 7 for the high-canard case. Results at 35, 45, and 55% spans, which are within the canard-tip span, show the development of the wing leading-edge vortex as indicated by the suction peaks. Figure 7 shows that the wing vortex strength is captured well by the computations. A previous study[4] showed that improvement in the

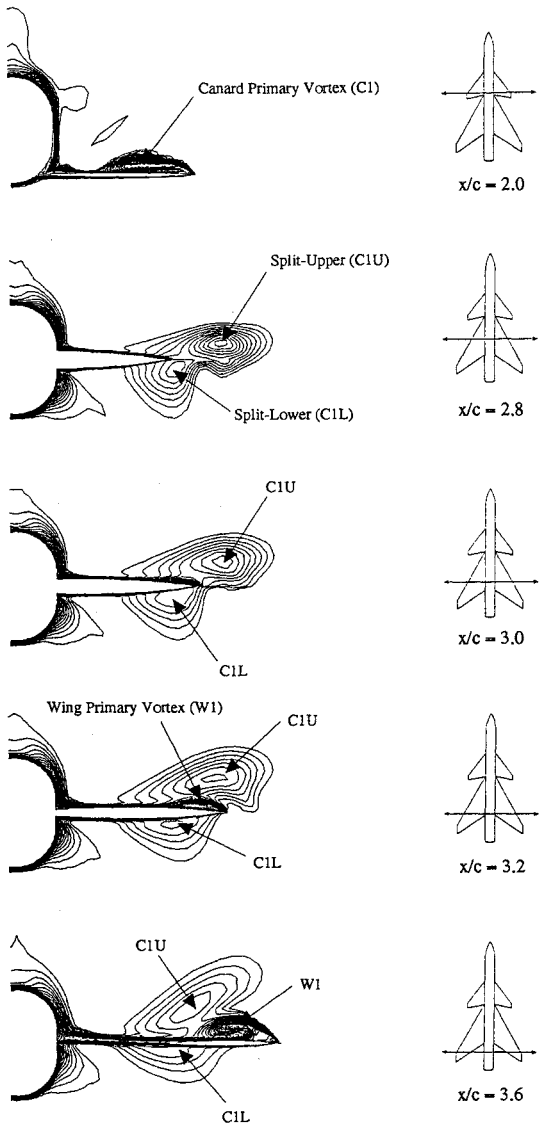

Fig. 11 Crossflow plane visualization of normalized total pressure contours for the low-canard configuration. $M_\infty = 0.90$, $\alpha = 8.55$ deg, $Re_{\bar{c}} = 1.52$ million.

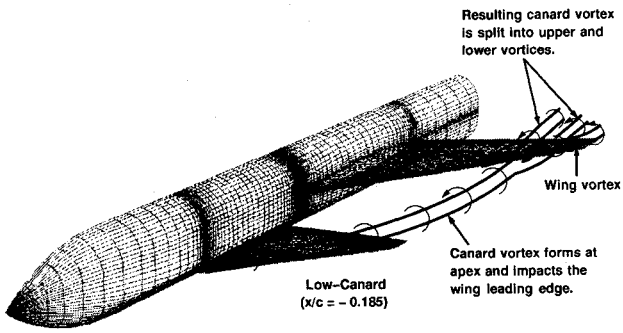

Fig. 12 Schematic of the canard and wing vortex trajectories for the low-canard configuration.

resolution of the wing surface pressure is obtained with further grid refinement.

Effects on Aerodynamic Performance

In order to predict the potential benefits of placing the canard in a non-coplanar (either high- or low-canard) configuration, a more detailed analysis of the lift and drag results is required. Polynomial curve fits through the computational and experimental results are used to determine the incremental lift and drag differences due to vertical positioning of the canard.

Figure 8a shows the effect of canard vertical position on the incremental change in lift coefficients ΔC_L at different angles of attack. The reference line ($\Delta C_L = 0.0$) is the computational or experimental C_L for the midcanard configuration. Although the absolute ΔC_L values are not exactly predicted by the computations, it is noted that relatively small values are being compared. The qualitative trends indicating the relative effects of canard vertical position are captured well by the computations. Both the computations and experiment show increased lift at higher angles of attack for the high-canard case. However, the low-canard ΔC_L curves show significant loss of lift as α is increased.

The incremental changes in drag coefficients ΔC_D given in Fig. 8b show that the high-canard configuration exhibits the best overall drag characteristics. At a higher C_L, the high-canard case has a lower C_D than both the mid- and low-canard cases. The results in Fig. 8 show clear evidence of an unfavorable canard-wing interaction for the low-canard configuration.

Differences in wing surface pressures between the high- and low-canard configurations are shown in Figs. 9a and 9b for $\alpha = 4.27$ and 8.55 deg, respectively. The upper and lower surface pressure distributions are given at three wing span stations for each angle of attack. All three stations are inboard of the canard-tip span line and, therefore, directly influenced by the high- or low-canard downwash. Results in Fig. 9 show that the relative canard and wing positions have a large effect on the level of canard-wing interaction.

At $\alpha = 4.27$ deg (Fig. 9a), small differences in wing surface pressures are observed. For the high-canard case, lower pressures on the upper surface near the wing leading edge indicate the possible formation of a leading-edge vortex. In the low-canard case, formation of the wing leading-edge vortex is inhibited due to the canard downwash and the relative positions of the canard and wing.

In Fig. 9b, the wing leading-edge vortex is clearly visible and contributes substantially to the lift of the high-canard configuration. However, even at this higher angle of attack, the low-canard results do not show evidence of a strong vortex on the inboard wing. In addition to inhibiting the formation of this vortex, the low-canard case also shows a substantial low pressure region on the wing lower surface. Both of these factors (absence of the wing vortex and low pressure on the wing lower surface) contribute to the loss of lift for the low-canard case observed in Figs. 5a and 8a.

Effects on Flowfield Structure

Further insight into the unfavorable nature of the low-canard configuration can be gained by examining the canard-wing flowfield structure. Figure 10 illustrates crossflow contours of stagnation pressures for the high- and low-canard configurations at $\alpha = 4.27$ deg. For each configuration, five streamwise stations are chosen to illustrate the development and convection of the canard and wing vortices. The high-canard results (Fig. 10a) show the formation of the canard vortex and its subsequent trajectory over the wing surface. At $x/\bar{c} = 3.2$ and 3.6, formation of the wing leading-edge vortex is observed. Although the vortex positions differ, the high-canard/wing vortex interaction has similar characteristics to that of the midcanard configuration studied in Ref. 4.

The low-canard case given in Fig. 10b shows a significantly different flowfield structure. Like the high-canard case, the low-canard vortex forms as visualized at $x/\bar{c} = 2.0$. However, due to the relative position of the low-canard to the wing and the canard-wing aerodynamic interaction, the subsequent canard vortex is convected under the wing surface. The low-canard vortex can therefore induce an unfavorable low pressure region on the wing lower surface. The formation of the wing vortex on the upper surface is again observed at $x/\bar{c} = 3.6$.

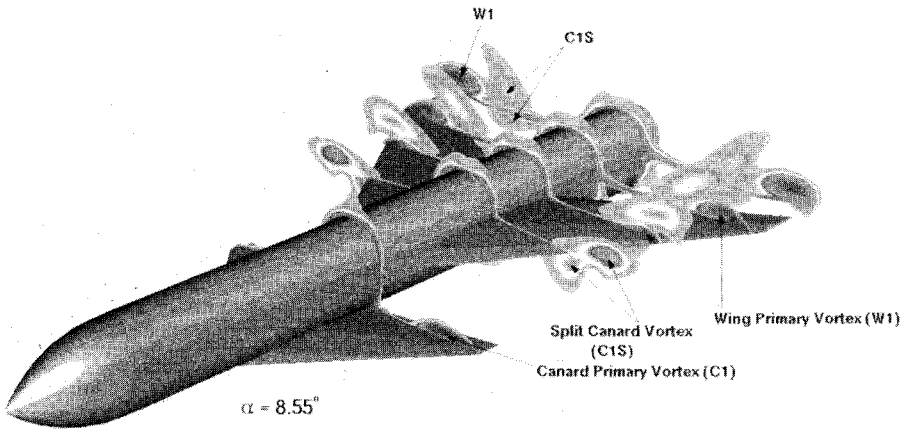

Fig. 13 Perspective view of normalized total pressure contours for the low-canard configuration. $M_\infty = 0.90$, $\alpha = 8.55$ deg, $Re_{\bar{c}} = 1.52$ million.

Figure 11 shows that at the higher angle of attack of 8.55 deg, the low-canard vortex interacts directly with the wing. The original low-canard vortex ($x/\bar{c} = 2.0$) splits into two (upper and lower canard) vortices upon impact with the wing leading edge ($x/\bar{c} = 2.8$). Further downstream at $x/\bar{c} > 3.2$, the split canard vortices continue to have the same rotational structure, but now exhibit independent trajectories. The canard lower vortex, with its counterclockwise rotational sense as viewed in the figure, tends to move inboard due to its proximity to the wing lower surface. The canard upper vortex, also with a counterclockwise rotation, is additionally influenced and moved inward by the formation of the wing vortex on the wing upper surface ($x/\bar{c} = 3.2$ and 3.6).

To visualize the results in Fig. 11 more clearly, a qualitative schematic of the canard-wing vortex trajectories for the low-canard case is given in Fig. 12. The low-canard vortex impacts the wing leading edge, and is split into the upper and lower vortices. The wing vortex forms on the wing upper surface and interacts with the canard upper vortex.

A summary perspective view of the low-canard vortex interaction with the wing is given in Fig. 13 for $\alpha = 8.55$ deg. Crossflow contours of stagnation pressures show the formation of the canard vortex, the splitting of the canard vortex by the wing, and the formation of the wing vortex on the outboard wing. The effect of this wing vortex on the canard upper-vortex trajectory is also clearly visible.

Concluding Remarks

A numerical simulation has been performed using the thin-layer Navier-Stokes equations to evaluate the steady flowfield about configurations with varying canard vertical positions. The capability to accurately model canard-wing aerodynamic interactions has been extended to account for the significant effects of canard vertical position on the configuration flowfield. The accuracy of this extension has been demonstrated by comparisons with available experimental force and moment measurements.

The results of this study show that, at low to moderate angles of attack, the high-canard configuration exhibits improved lift and drag over the midcanard case. However, due to the interaction between the low-canard vortex and the wing surface, unfavorable lift and drag characteristics for the low-canard configuration are evident as angle of attack is increased. At low angles of attack, the low-canard vortex passes under the wing surface and can induce lower pressures on the wing lower surface. At higher angles of attack, the canard vortex is split by the wing surface into upper and lower vortices. Toward the outboard wing, the wing vortex induces a large inward movement of the canard upper vortex.

These findings both correlate with, and provide an explanation for, earlier experimental results. This study also suggests that detailed investigations are required to determine optimum canard positioning for given configurations.

References

[1]Yeh, D. T., George, M. W., Clever, W. C., Tam, C. K., and Woan, C. J., "Numerical Study of the X-31 High Angle-of-Attack Flow Characteristics," AIAA Paper 91-1630, June 1991.

[2]Modin, K. E., and Clareus, U., "Aerodynamic Design Evolution of the SAAB JAS 39 Gripen Aircraft," AIAA Paper 91-3195, Sept. 1991.

[3]Kehoe, M. W., Bjarke, L. J., and Laurie, E. J., "An In-Flight Interaction of the X-29A Canard and Flight Control System," NASA TM 101718, April 1990.

[4]Tu, E. L., "Navier-Stokes Simulation of a Close-Coupled Canard-Wing-Body Configuration," *Journal of Aircraft*, Vol. 29, No. 5, 1992, pp. 830–838.

[5]Gloss, B. B., and McKinney, L. W., "Canard-Wing Lift Interference Related to Maneuvering Aircraft at Subsonic Speeds," NASA TM X-2897, Dec. 1973.

[6]Gloss, B. B., "The Effect of Canard Leading-Edge Sweep and Dihedral Angle on the Longitudinal and Lateral Aerodynamic Characteristics of a Close-Coupled Canard-Wing Configuration," NASA TN D-7814, Dec. 1974.

[7]Gloss, B. B., "Effect of Canard Location and Size on Canard-Wing Interference and Aerodynamic-Center Shift Related to Maneuvering Aircraft at Transonic Speeds," NASA TN D-7505, June 1974.

[8]Lacey, D. W., "Aerodynamic Characteristics of the Close-Coupled Canard as Applied to Low-to-Moderate Swept Wings, Volumes 1–4," David W. Taylor Naval Ship Research and Development Center Rept., DTNSWDC-79/001-004, Jan. 1979.

[9]Gloss, B. B., and Washburn, K. E., "Load Distribution on a Close-Coupled Wing Canard at Transonic Speeds," *Journal of Aircraft*, Vol. 15, No. 4, 1978, pp. 234–239.

[10]Gloss, B. B., and Washburn, K. E., "A Study of Canard-Wing Interference Using Experimental Pressure Data at Transonic Speeds," NASA TP 1355, Jan. 1979.

[11]Er-El, J., and Seginer, A., "Vortex Trajectories and Breakdown on Wing-Canard Configurations," *Journal of Aircraft*, Vol. 22, No. 8, 1985, pp. 641–648.

[12]Calarese, W., "Vortex Interaction on a Canard-Wing Configuration," Air Force Wright Aeronautical Lab., AFWAL-TR-86-3100, Wright-Patterson AFB, Dayton, OH, Oct. 1986.

[13]Oelker, H., and Hummel, D., "Investigations on the Vorticity Sheets of a Close-Coupled Delta-Canard Configuration," *Journal of Aircraft*, Vol. 26, No. 7, 1989, pp. 657–666.

[14]Holst, T. L., Kaynak, U., Gundy, K. L., Thomas, S. D., and Flores, J., "Numerical Solution of Transonic Wing Flows Using an Euler/Navier-Stokes Zonal Approach," *Journal of Aircraft*, Vol. 24, No. 1, 1987, pp. 17–24.

[15]Flores, J., "Convergence Acceleration for a Three-Dimensional Euler/Navier-Stokes Zonal Approach," *AIAA Journal*, Vol. 24, No. 9, 1986, pp. 1441, 1442.

[16]Tu, E. L., "Effect of Canard Deflection on Close-Coupled Canard-Wing-Body Aerodynamics," AIAA Paper 92-2602, June 1992.

[17]Kaynak, U., Holst, T. L., and Cantwell, B. J., "Computation of Transonic Separated Wing Flows Using an Euler/Navier-Stokes Zonal Approach," NASA TM 88311, July 1986.

[18]Flores, J., Reznick, S. G., Holst, T. L., and Gundy, K. L., "Transonic Navier-Stokes Solutions for a Fighter-Like Configuration," *Journal of Aircraft*, Vol. 25, No. 10, 1988, pp. 875–881.

[19]Flores, J., and Chaderjian, N. M., "Zonal Navier-Stokes Methodology for Flow Simulation About a Complete Aircraft," *Journal of Aircraft*, Vol. 27, No. 7, 1990, pp. 583–590.

[20]Flores, J., Tu, E. L., Anderson, B., and Landers, S., "A Parametric Study of the Leading Edge Attachment Line for the F-16XL," AIAA Paper 91-1621, June 1991.

[21]Baldwin, B. S., and Lomax, H., "Thin Layer Approximation and Algebraic Model for Separated Turbulent Flows," AIAA Paper 78-257, Jan. 1978.

[22]Degani, D., and Schiff, L. B., "Computation of Turbulent Supersonic Flows Around Pointed Bodies Having Crossflow Separation," *Journal of Computational Physics*, Vol. 66, No. 1, 1986, pp. 173–196.

[23]Luh, R. C., Pierce, L., and Yip, D., "Interactive Surface Grid Generation," AIAA Paper 91-0796, Jan. 1991.

[24]Sorenson, R. L., "The 3DGRAPE Book: Theory, Users' Manual, Examples," NASA TM 102224, July 1989.

[25]Klopfer, G. H., and Molvik, G. A., "Conservative Multizone Interface Algorithm for the 3-D Navier-Stokes Equations," AIAA Paper 91-1601, June 1991.